

Scaling Properties of Polycrystalline Graphene: A Review

Andreas Isacsson¹, Aron W. Cummings², Luciano Colombo^{2,3,4}, Luigi Colombo⁵, Jari M. Kinaret¹, and Stephan Roche^{2,6}

¹Department of Physics, Chalmers University of Technology, SE-412 96 Gothenburg, Sweden

²Catalan Institute of Nanoscience and Nanotechnology (ICN2), CSIC and the Barcelona Institute of Science and Technology Campus UAB, 08193 Bellaterra, Barcelona, Spain

³Dipartimento di Fisica, Università di Cagliari, Cittadella Universitaria, 09042 Monserrato (Ca), Italy

⁴Institut de Ciència de Materials de Barcelona (ICMAB–CSIC), 08193 Bellaterra, Barcelona, Spain

⁵Texas Instruments Incorporated, 13121 TI Boulevard, MS-365, Dallas, Texas 75243, United States

⁶ICREA, Institució Catalana de Recerca i Estudis Avançats, 08070 Barcelona, Spain

E-mail: andreas.isacsson@chalmers.se

19 November 2021

Abstract. We present an overview of the electrical, mechanical, and thermal properties of polycrystalline graphene. Most global properties of this material, such as the charge mobility, thermal conductivity, or Young's modulus, are sensitive to its microstructure, for instance the grain size and the presence of line or point defects. Both the local and global features of polycrystalline graphene have been investigated by a variety of simulations and experimental measurements. In this review, we summarize the properties of polycrystalline graphene, and by establishing a perspective on how the microstructure impacts its large-scale physical properties, we aim to provide guidance for further optimization and improvement of applications based on this material, such as flexible and wearable electronics, and high-frequency or spintronic devices.

Submitted to: *2D Mater.*

1. Introduction

The macroscopic physical properties of polycrystalline materials depend crucially on the structure and distribution of crystallites and grain boundaries. These, in turn, depend on the synthesis method used. To produce high-quality and large-scale two-dimensional materials such as graphene, transition metal dichalcogenides, and hexagonal boron nitride, the manufacturing method of choice has primarily been chemical vapor deposition (CVD). CVD-grown graphene and related materials exhibit a polycrystalline morphology, consisting of a patchwork of individual grains which coalesce to form one-dimensional boundaries separating domains of different crystalline orientations. Although graphene crystal growth has been at the center of much research over the past decade, large flat perfect single crystals remain fairly elusive, and the resulting structures depend on the details of the fabrication process. Large-area graphene grown by CVD on metals such as Cu, Cu-Ni, Pt, Ru, and Ir, is typically polycrystalline with grain sizes ranging from a few hundred nanometers to several centimeters in diameter, with a roughness that mimics that of the metal substrate. Graphene films grown on SiC, on the other hand, have shown excellent flatness but replicate the crystallographic step structure of the SiC single crystals, which leads to few-layer graphene or edge defects.

For understanding macroscopic properties, studying individual boundaries is thus not sufficient, and one must also take a more global view of the effects of the polycrystalline structure, e.g. grain size distribution. In this review, we will therefore first present the essentials of grain boundary geometries, which are characterized principally by non-hexagonal rings such as pentagons and heptagons. Afterwards, the average grain size will be taken as a reference parameter to analyse the scaling of charge transport, mechanical properties, and thermal conduction as a function of geometry, contrasting when possible the theoretical predictions with available experimental data.

2. Grain boundaries in graphene

Considerable effort has so far been spent on understanding the structure and energetics of single grain boundaries (GBs) separating two grains. Macroscopic characterization of such a boundary requires knowledge of the misorientation angle α between the two

regions (left and right) separated by the grain boundary, the direction ψ of the GB, and a translation vector that gives the relative displacement between the lattices on different sides of the boundary [1]. In the simplest case, the GB is symmetric and forms a mirror symmetry plane between the two crystalline regions. This requires that the crystal orientations to the left and right of the grain boundary are $\alpha_L = \psi - \alpha$ and $\alpha_R = \psi + \alpha$ ‡. A symmetric grain boundary exhibits periodicity with period $(n^2 + nm + m^2)^{1/2}$ where n and m give the direction of the boundary in terms of the basis vectors of the left or right region. For small misorientation angles α , a symmetric grain boundary can be thought of as arising from a periodic series of parallel edge dislocations terminating at the boundary.

Microscopically, grain boundaries in graphene result in deviations from the regular hexagonal structure of the graphene lattice. In crystalline membranes, an individual positive or negative disclination cannot be viewed as a point defect as it results in a global warping with a logarithmically diverging energy [2]. Hence, pairs of positive and negative disclinations are needed [2]. In graphene, edge dislocations are thus typically terminated by pentagon-heptagon pairs [3–5]. These disclination dipoles conserve the three-fold coordination of each carbon atom and yield a low energy cost for the defect (see Fig. 1a).

A small misorientation angle α results in widely separated pentagon-heptagon pairs, while a large α requires the pairs to be close to each other (see Fig. 1b). As shown in [6, 7], in order to match periodic boundary conditions (needed for modeling by atomistic simulations) only some specific orientations are possible, corresponding to $\alpha = 3.0^\circ, 4.1^\circ, 8.2^\circ, 10.9^\circ$, and 16.1° . However, for a generic large α the boundary must assume a more complicated structure than simple pentagon-heptagon pairs. In the general case of an asymmetric grain boundary, periodicity only occurs if certain commensurability conditions are met, and the resulting period is typically much longer, which usually results in a higher energy cost per length of the boundary and a more complicated analysis [7, 8].

To accommodate the strain generated by the GB, out-of-plane corrugation of the graphene sheet typically occurs [2–4]. Figure 1c shows C-atom displacements perpendicular to the graphene plane.

‡ Some references use another definition of crystalline axes in the two regions, which results in $\alpha_R \rightarrow -\alpha_R$ and $\alpha = (\alpha_L + \alpha_R)$ rather than our convention where $\alpha = (\alpha_R - \alpha_L)/2$

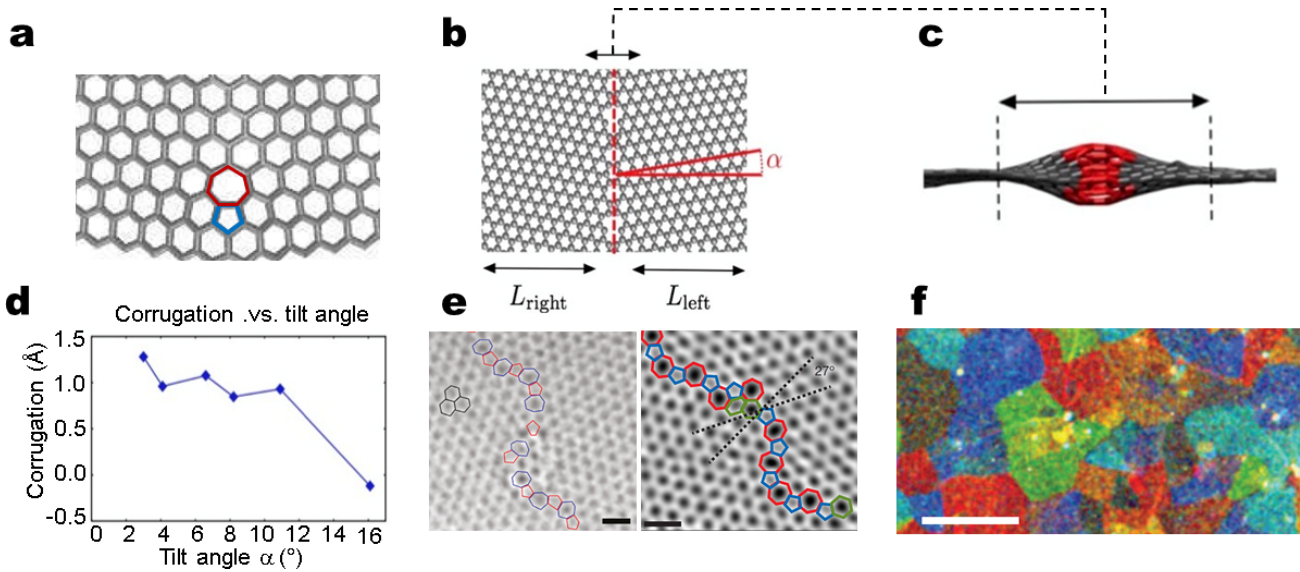


Figure 1. Structure of grain boundaries in polycrystalline graphene. **a.** A disclination in graphene consists of a pentagon-heptagon pair, which maintains the three-fold coordination. **b.** In-plane structure of a symmetric model grain boundary in graphene, obtained by tilting two sheets of equal length by an angle $\alpha = 8.2^{\circ}$. **c.** Out-of-plane structure showing corrugation occurring nearby the grain boundary, as predicted by MD simulations. In low-angle symmetric tilt grain boundaries, out-of-plane buckling (warping) reduces the energy associated with boundary stress. **d.** Corrugation as function of the tilt angle. **e.** Meandering grain boundaries imaged by AC-TEM. In CVD-grown graphene, the boundaries are typically neither symmetric nor straight, but have more complex geometry [adapted with permissions from ACS Nano 5 2142, copyright (2011) and from Macmillan Publishers Ltd: Nature 469, 389, copyright (2011)]. **f.** False-color image of polycrystalline graphene. The global properties of polycrystalline graphene are determined not only by the microscopic properties of the grain boundaries, but also by the distribution of grain sizes and crystal orientations [adapted from Science 340, 1073, copyright (2013). Reprinted with permission from AAAS].

The buckling amplitude, decreasing with increasing tilt angle α is typically $\sim 1.0 \text{ \AA}$ (see Fig. 1d), in good agreement with available data [9, 10]. The width of the buckled region, corresponding in turn to the GB thickness, is as large as 3-4 \AA , and can be either symmetrical or antisymmetrical around the disclination dipole [11].

While many theoretical analyses to date have focused on grain boundary constructions with rather short periodicities, grain boundary characterizations using transmission electron microscopy [12, 13] have revealed more complicated structures (see Fig. 1e, f). Although the fundamental units of these boundaries are pentagon-heptagon pairs, they tend to be meandering. Recently, Rasool, Ophus and co-workers carried out large-scale experimental characterization and molecular dynamics simulations of GBs with lengths up to 200 nm [14, 15]. For isolated grain boundaries, the agreement between the molecular dynamics simulations and experimental measurements is quite good in terms of the atomic structure and mechanical properties [14]. However, very little work has been carried out on grain boundary junctions where three or more crystalline regions come together and on the statistics of crystallite size and orientation. These properties depend to a large extent on the details of the fabrication process.

3. Charge transport in polycrystalline graphene

The first electrical transport measurements on isolated graphene were made in single-crystal flakes on silicon dioxide substrates. The subsequent introduction of graphene grown by CVD provided the opportunity to measure large-area films [16], but these films have been predominantly polycrystalline in comparison to the device size. In general, GBs in semiconductor materials are detrimental to charge transport [17], and for this reason the semiconductor industry favors high-quality single-crystal materials with a low density of extended and point defects to minimize device degradation. Indeed, much of the success of the semiconductor industry over the years has arisen from the ability to grow a large volume of low-defect single crystals and thin films, out of materials including Si, III-V, II-VI, and IV-IV compounds.

Graphene, unlike the semiconductors used for electronic devices, is a semimetal and thus it is less clear if extended defects have a large effect on transport properties. Therefore, because of its promise for large-area electronic applications, a detailed understanding of the electrical transport properties of polycrystalline graphene is crucial. To this end, a great deal of experimental [13, 18–27] and theoretical [7, 28–38] effort

has been devoted to studying charge transport across individual graphene grain boundaries, and several reviews have already discussed this topic in great detail [5, 26, 39]. Therefore, here we briefly summarize the main features of electrical transport across individual graphene GBs before shifting our focus to a more global perspective of charge transport in polycrystalline graphene.

3.1. Electrical resistivity of individual grain boundaries

Four-terminal measurements across individual GBs show an enhanced electrical resistance compared to the surrounding grains, $R_{\text{total}} = R_{\text{grains}} + R_{\text{GB}}$ [18–21, 23–27]. The origin of this enhanced resistance has been probed with scanning tunneling spectroscopy (STS), and these measurements have revealed that GBs tend to be n-doped compared to the surrounding grains, such that they act as an electrical potential barrier to charge transport [40, 41]. Magnetotransport measurements [18, 19, 42], numerical simulations [43], and STS measurements [40, 41] have shown that GBs also induce weak localization, indicating that they are a source of intervalley scattering. Additionally, temperature-dependent measurements have shown that R_{GB} is independent of temperature, providing further support for the hypothesis that scattering at the GBs is dominated by structural defects and impurities [18–20].

The resistance of an individual graphene GB can be written as $R_{\text{GB}} = \rho_{\text{GB}}/W$, where ρ_{GB} is the GB resistivity and W is the device width (or equivalently, the GB length). The GB resistivity thus provides an intrinsic measure of the charge transport properties across the GB, independent of the device or measurement technique. Beyond four-terminal electrical measurements, the resistivity of individual GBs has been measured using a.c. electron force microscopy (AC-EFM) [13], four-point scanning tunneling potentiometry (STP) [21], and Joule expansion microscopy [23]. The average ρ_{GB} of a series of polycrystalline samples can also be extracted by measuring the sheet resistance of each sample as a function of the average grain size [44–49] and then fitting to a simple ohmic scaling law, $R_{\text{S}} = R_{\text{S}}^0 + \rho_{\text{GB}}/l_{\text{G}}$, where R_{S} is the sheet resistance of the polycrystalline sample, R_{S}^0 is the sheet resistance within the grains, and l_{G} is the average grain size [26].

A summary of the values of ρ_{GB} that have been reported in the literature is shown in Fig. 2. Markedly, ρ_{GB} spans more than three orders of magnitude, from less than 0.1 up to 100 $\text{k}\Omega\text{-}\mu\text{m}$. To account for this spread of values, there are several factors that should be considered. Factors that impact the intrinsic value of the GB resistivity include the structural quality

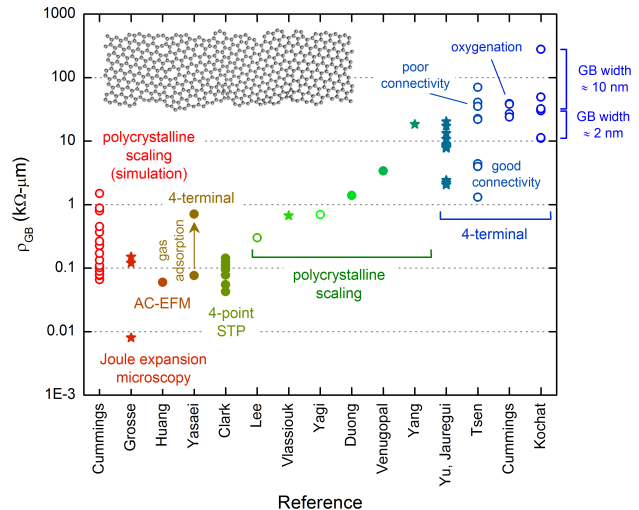


Figure 2. Summary of the values of grain boundary resistivity (ρ_{GB}) extracted from the literature [13, 18–21, 23, 25–27, 44–49]. Each value is labeled according to the measurement technique, and additional notes have been included where appropriate. Open circles represent measurements made at the charge neutrality point, closed circles represent measurements made far from the charge neutrality point, and \star 's are for measurements where the position of the Fermi level is unknown. The spread of simulation results is due to the impact of chemical functionalization on the value of ρ_{GB} .

of the GB, the position of the Fermi level, and the measurement technique. Other factors that can alter the GB resistivity are related to the cleanliness of the device, such as if the graphene was protected by a gate dielectric or if an exposed graphene film was measured in air or in vacuum.

Tsen *et al* showed that poorly-connected GBs can significantly enhance ρ_{GB} , in their case by one order of magnitude [20], and this behavior has also been seen in numerical simulations [50]. Kochat *et al* also showed a strong correlation between the GB quality and its resistivity, where GBs with a wide region of disorder were more resistive than narrower GBs [27]. Meanwhile, the numerical simulations in Fig. 2 were made with perfectly connected polycrystalline samples, and thus yielded relatively low values of ρ_{GB} [26].

When determining the GB resistivity, control of the Fermi level is also important, as four-terminal measurements have shown that the value of ρ_{GB} can vary by one order of magnitude as a function of gate voltage, with the maximum occurring at the charge neutrality point (CNP) [20, 27]. In Fig. 2, open circles represent measurements with the Fermi level at the CNP, closed circles are for measurements where the Fermi level is far from the CNP, and \star 's are for measurements where the Fermi level is unknown. In general, the largest measured values of ρ_{GB} , on the far right of Fig. 2, were all made at the CNP, while the lowest measured values of ρ_{GB} were made far from the

CNP. Scaling the lowest measured values of ρ_{GB} by a factor of 10 brings them into the range of the four-terminal measurements made at the CNP.

The measurement technique also appears to have some impact on the estimated value of the GB resistivity. In particular, the values of ρ_{GB} extracted from the scaling law tend to be lower than those from four-terminal measurements, even at the CNP. When considering electrical transport through a large polycrystalline sample, charge will flow through a series of parallel conducting paths, and the sheet resistance will be determined by the lowest resistance path. For this reason, the value of ρ_{GB} extracted from the scaling law represents the lower end of the range of GB resistivities present in the sample, and not the average value. When considering all three factors together, it appears that the resistivity of well-connected GBs, measured at the CNP, typically falls in a range around 1 k Ω - μm .

While GBs by themselves may not always give rise to significant scattering, the adsorption and reaction of adsorbates or impurities can adversely impact the electrical transport. While this may be detrimental for high-performance electronic devices, it could be advantageous for gas sensing applications [51, 52]. Four-terminal measurements of highly-resistive GBs showed that oxygenation can vary ρ_{GB} by a factor of two [26], while adsorption of dimethyl methylphosphonate gas molecules increased the resistivity of a low-resistance GB by one order of magnitude [25]. Numerical calculations also revealed a strong variation of ρ_{GB} with chemical functionalization [26], indicated by the spread of values on the far left of Fig. 2. In contrast to these results, recent work by Gao *et al* demonstrated a room temperature mobility of nearly 5000 cm²/V-s for polycrystalline samples with an average grain size on the order of 100 nm [53]. These promising results highlight the need to design experiments that can separate the intrinsic effect of the GBs from extrinsic factors like surface cleanliness. The dry transfer method recently reported by Banszerus *et al*, which yielded single-grain CVD graphene with mobilities up to 350,000 cm²/V-s, is one such approach [54].

Beyond impeding charge transport, individual graphene GBs can impact the electrical properties of polycrystalline graphene in other ways. For example, Joule expansion microscopy measurements have revealed strong Joule heating localized at graphene GBs, which can be many times larger than Joule heating in the grains. This has important implications for the reliability of graphene devices, as localized device failure could occur without a significant increase in the average device temperature [23]. Other measurements have shown that electrical

noise is greatly enhanced by graphene GBs, which is detrimental for low-noise devices but may be useful for sensor applications [27].

3.2. Global transport properties of polycrystalline graphene

While knowledge of the resistivity of individual GBs is valuable from both a fundamental point of view and for particular applications, it is also important to have a clear picture of the global charge transport properties of polycrystalline graphene. This is especially important for large-area devices that utilize this material, such as flexible transparent electrodes. In polycrystalline graphene, charge transport is ultimately limited by two sources – scattering at the GBs, and scattering within the graphene grains. The competition between these two sources of resistance is simply captured by the ohmic scaling law mentioned above, $R_{\text{S}} = R_{\text{S}}^0 + \rho_{\text{GB}}/l_{\text{G}}$. For samples with large grains, the sheet resistance will be dominated by that of the grains, R_{S}^0 , and R_{S} will be independent of the grain size. For small-grained samples, R_{S} will be dominated by ρ_{GB} and will scale inversely with the grain size. The crossover from grain- to GB-dominated behavior occurs at a grain size of $l_{\text{G}} \approx \rho_{\text{GB}}/R_{\text{S}}^0$. This general behavior is shown by the solid gray line in Fig. 3, where we plot the sheet resistance as a function of the grain size assuming $R_{\text{S}}^0 = 300 \Omega/\square$ and $\rho_{\text{GB}} = 0.3 \text{ k}\Omega\text{-}\mu\text{m}$.

In Fig. 3 we also plot a selection of values of sheet resistance vs. grain size that have been reported in the experimental literature. Most measured values follow a general inverse scaling between R_{S} and l_{G} , and the slope of this scaling can provide information about the relative values of ρ_{GB} and R_{S}^0 . For example, the shallow scaling reported by Yagi *et al* [46] suggests a low value of $\rho_{\text{GB}} = 0.7 \text{ k}\Omega\text{-}\mu\text{m}$, but a relatively large grain sheet resistance of $R_{\text{S}}^0 = 6 \text{ k}\Omega/\square$. However, the measurements of Yang *et al* [49], while similar in magnitude, show a much steeper slope, giving a large value of $\rho_{\text{GB}} = 18 \text{ k}\Omega\text{-}\mu\text{m}$ but a smaller $R_{\text{S}}^0 = 600 \Omega/\square$. The measurements of Duong *et al* [45], Lee *et al* [47], and Venugopal [48] all reveal low values of $R_{\text{S}}^0 = 100\text{-}300 \Omega/\square$, while those of Lee *et al* have the smallest GB resistivity, 0.3 k Ω - μm [47]. It should be noted that for the values reported by Vlasiouk *et al*, Raman spectroscopy was used to determine the size of defect-free regions, but this technique does not distinguish between disorder in the grains and disorder arising from the GBs [44]. As mentioned before, the spread in the numerical calculations of the sheet resistance (open squares) is due to varying degrees of chemical functionalization applied to the GBs [26].

It is clear that minimizing the impact of GBs is important for electronic applications of polycrystalline graphene, and today it is possible to grow single

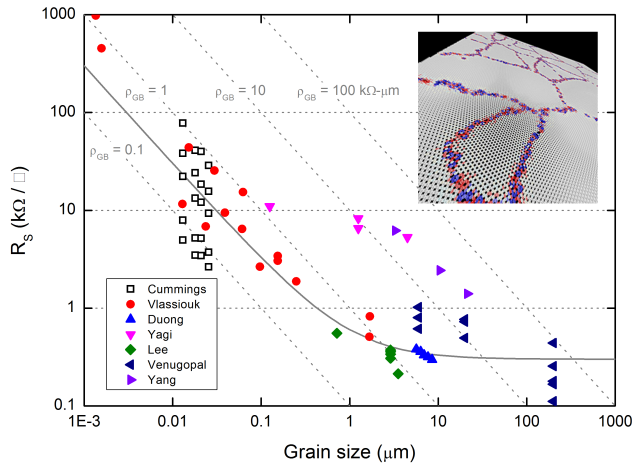


Figure 3. Summary of the measured values of polycrystalline graphene sheet resistance as a function of average grain size. The solid symbols are experimental measurements [44–49] and the open squares are numerical calculations from Ref. [26]. The grey solid line shows the behavior of the ohmic scaling law, $R_S = R_S^0 + \rho_{GB}/l_G$, assuming $R_S^0 = 300 \Omega/\square$ and $\rho_{GB} = 0.3 \text{ k}\Omega\text{-}\mu\text{m}$.

graphene grains with diameters on the order of centimeters [55–57]. However, there is a significant tradeoff between grain size, the required temperature, and the growth time in the CVD process, and when it comes to industrial applications these growth conditions should be minimized [58]. By understanding the scaling of the sheet resistance, one can determine the grain size needed for a particular application. For example, with a growth process that yields a grain sheet resistance of $R_S^0 = 100 \Omega/\square$ and a GB resistivity of $\rho_{GB} = 1 \text{ k}\Omega\text{-}\mu\text{m}$, the grains only need to be larger than $\rho_{GB}/R_S^0 = 10 \mu\text{m}$ for the contribution of the GBs to no longer matter. Thus, depending on the requirements, centimeter-sized grains may be unnecessary. This was recently demonstrated by Samsung and its collaborators, whose rapid thermal CVD process yielded polycrystalline graphene samples with a sheet resistance that was constant over grain sizes in the range of 1–10 μm [58].

In addition to direct charge transport, polycrystalline graphene has also been studied for its application to quantum Hall metrology. In single-crystal graphene, clear signatures of the quantum Hall effect have been measured at room temperature [59], owing to the relatively large splitting of the two lowest Landau levels. This makes graphene quite promising for the establishment of new resistance standards, as measurements can be made at higher temperatures and lower magnetic fields than those in traditional two-dimensional electron gases [60, 61]. However, in polycrystalline graphene the quantum Hall measurements are less ideal, with a degradation of the precision of the quantum Hall plateaus and the development of a finite

longitudinal conductivity [42, 62, 63]. Various numerical simulations have shown that GBs can short circuit the quantum Hall measurement [43, 63–65], and the network of GBs provides a path for percolating transport through the bulk of the material [43]. Very small grains can also impede the onset of the quantum Hall regime until the magnetic field becomes large enough such that $l_B < l_G$, where $l_B = \sqrt{\hbar/eB}$ is the magnetic length [43, 53]. In general, these results indicate that GBs should be avoided in order to achieve high-precision quantum Hall measurements.

Polycrystalline graphene has also been considered for thermoelectric applications. The figure of merit of a thermoelectric material is given by $ZT = S^2\sigma T/\kappa$, where T is the temperature, S is the Seebeck coefficient, and σ (κ) is the electrical (thermal) conductivity. ZT is a measure of the efficiency of a thermoelectric engine, and its value can be tuned by separately tuning S , σ , and κ . Recent theoretical work has predicted that an individual GB can significantly enhance the ZT of graphene at the CNP, primarily through an enhancement of the Seebeck coefficient [66]. However, simulations of large-area polycrystalline graphene samples are less optimistic, as they show that σ and κ scale similarly with the grain size [50, 67–69], while the Seebeck coefficient is reduced compared to pristine graphene [70]. Together, these results suggest an overall reduction of ZT compared to single-grain graphene.

Finally, it is important to note that beyond the microstructure, the process of device fabrication can also have a strong impact on electrical transport. Exfoliated and CVD graphene are usually transferred onto a dielectric substrate using scotch tape or organic compounds such as PMMA, resulting in physisorbed or chemisorbed residues on the graphene surface [71]. If the graphene sheet contains point defects, dislocations, grain boundaries, or wrinkles, the residues can attach more easily [72]. In fact, during the initial stages of graphene device fabrication, dielectric films were usually difficult to deposit on unfunctionalized or “clean” graphene surfaces, and several techniques were introduced to overcome this problem [73–75]. The ability to deposit the dielectric uniformly on graphene protected the films from ambient adsorbates, which can have a significant effect on the transport properties [76], but these processes also introduced organics, ozone, metals, or metal oxides that tended to degrade the mobility in comparison to devices without a top gate [77, 78]. Therefore, when analyzing graphene mobility data it is critically important to know the quality of the dielectric substrate, the crystallinity of the graphene, and the gate dielectric. This was clearly demonstrated by the use of hexagonal boron nitride (h-BN) as a substrate material and gate dielectric [79],

which can lead to very high mobilities in both single-crystal and bi-layer graphene [80, 81]. In cases where the surface of graphene is not exposed to any organic compounds during the transfer process, the mobility is also greatly improved [82] although in this case perhaps the benefit is also associated with low strain in the graphene films transferred using h-BN [83].

4. Mechanical properties of polycrystalline graphene

Graphene is often noted for its remarkable mechanical properties, including its large elastic modulus and high fracture strength. For a low-dimensional material such as graphene it is natural to expect grain boundaries to greatly alter elastic constants and the fracture strength. Several experimental, as well as theoretical works, suggest that individual grain boundaries can possess mechanical properties close to those of pristine graphene [5, 15, 84]. However, other works, with a more global view on polycrystalline graphene, indicate that these properties can strongly depend on grain size l_G and system size L . In particular, the ratio l_G/L may play an important role, and few works have so far been able to access the limit of $l_G/L \ll 1$, which is of importance for many large-scale applications.

4.1. Influence on elasticity

The elastic properties of graphene are commonly studied experimentally by means of nanoindentation experiments [85]. For numerical studies, molecular dynamics (MD) is typically required as system sizes are in general too large for density functional theory (DFT) to be practical. In a nanoindentation measurement, the graphene devices have the form of a micron-sized suspended circular drum. By pressing down with an atomic force microscope (AFM) while recording applied force and tip deflection, the elastic properties are deduced. While experimental devices have micron linear dimension, numerical simulations are limited to much smaller systems ($\lesssim 100$ nm). In MD studies, the mechanical properties are probed by recording the stress as the system is uni- or bi-axially strained. This should be contrasted with the nanoindentation experiments where the strain is typically non-uniform even for a pristine sheet and where the details of the AFM tip shape may influence the results. For pristine graphene, both numerics (MD/DFT) and indentation experiments show good agreement, yielding a Young's modulus either quoted as a 2D entity $E_{2D} \approx 340$ N/m or as the equivalent 3D modulus $E_{3D} \approx 1$ TPa [85, 86]. The two are related through the interlayer spacing of graphite (3.35 Å).

For polycrystalline sheets, however, there is a larger discrepancy between reported values. On the

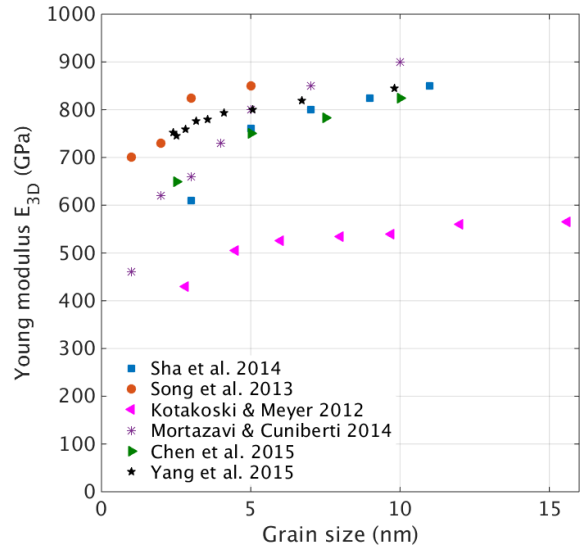


Figure 4. Young's modulus for polycrystalline graphene as function of linear grain size as obtained from MD simulations [90–95]. While there is a large discrepancy in absolute numbers, all studies show a trend of increasing stiffness with grain size.

experimental side, one complication arises from the different methods of fabrication and transfer. Not only does this yield samples with different quality of grain boundaries and different amounts of pre-stress, but also the amount of wrinkling differs between samples. Wrinkling or buckling can be either the result of the fabrication-transfer process or due to the boundaries themselves, which alleviate the extra strain incurred by the defects. This causes a softening of the Young's modulus for small grains. On the theoretical side, the choice of interaction potential and grain boundary geometry can greatly influence the results.

Theoretical studies of the simplest geometry, graphene sheets containing a single straight grain boundary [87–89], found values around $E_{3D} \sim 800$ GPa. This was confirmed by nanoindentation measurements using an AFM tip to press down on polycrystalline suspended CVD graphene drums which showed, within statistical error, a value of $E_{3D} \sim 1$ TPa [84]. Although the spread in measured elastic constants was larger for polycrystalline graphene than for pristine graphene, the average value was still in agreement with that of pristine graphene. In the experiments by Lee *et al* [84], the diameter of the suspended graphene drums was similar to the grain size.

Both the theory [87–89] and experiments [84] essentially studied local grain boundary properties, i.e they were in the regime $l_G/L \lesssim 1$. However, those findings are in contrast to theory taking into account more natural grain boundary geometries. Such simulations typically result in lower values

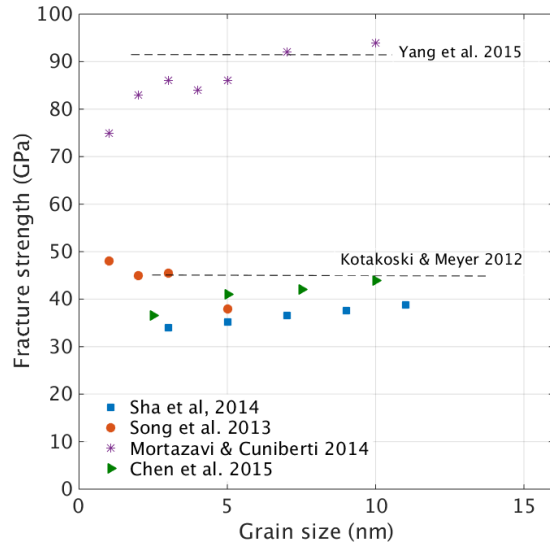


Figure 5. Fracture strength obtained by MD as a function of grain size from references [91–93,95]. While three of the studies [92,93,95] show increasing fracture strength with increasing grain size, the results of Song *et al* [91] show the opposite trend. The grain-size-independent results by Kotakoski and Meyer [90] and Yang *et al* [94] are shown as dashed lines.

for E_{3D} [90–95]. In particular, Kotakoski and Meyer [90], who performed large-scale MD simulations on polycrystalline graphene, found significantly lower values of the Young’s modulus $E_{3D} \sim 600$ GPa. While smaller values were obtained experimentally using indentation measurements [13, 96] with values $E_{3D} \sim 150$ GPa, these were attributed to the out-of plane buckling associated with the grain boundaries. Finally, not only grain boundaries may affect the elastic properties. As highlighted by nanoindentation measurements [97, 98] on graphene with controlled creation of defects, the type of defects and their concentration can also impact the results.

As in 3D macroscopic materials, the characteristic grain size l_G plays an important role. From MD simulations, a clear grain-size dependence of the elastic modulus has been found, with E_{3D} increasing upon increasing the grain size [90–95] (see Fig. 4). In order to have a well-defined value of an elastic property, it is desirable that it be measured for a system size $L \gg l_G$. For practical reasons, simulating structures with linear dimensions L much larger than the characteristic grain sizes has remained prohibitive except for very small grains (~ 1 nm), and most studies have not studied the scaling with l_G/L . Also, nanoindentation studies are performed on micrometer-sized systems comparable to the grain sizes ($L \sim l_G \sim 1 \mu\text{m}$), and reporting the ensemble-averaged values over many devices. There is, however, currently no experimental work covering the case $L \gg l_G \sim 1 \mu\text{m}$ for the Young’s modulus.

4.2. Fracture strength

Monocrystalline graphene is predicted to have an extraordinary fracture strength of 110 - 130 GPa [84, 88, 99, 100]. In presence of grain boundaries it is natural to expect that this strength is diminished. However, using MD, it was shown [87] that in contrast to this expectation, higher-angle tilt grain boundaries with a higher density of defects (heptagon-pentagon pairs) can be as strong as mono-crystalline graphene, while low-angle boundaries with lower defect concentrations showed a reduction in fracture strength. This behaviour derives from the dipolar stress profile around individual pentagon-heptagon pairs surrounded by hexagons, with tensile stress on the heptagon side and compressive stress on the pentagon side (see Fig. 1c). With an increased density of aligned pentagon-heptagon pairs, stress cancellation from adjacent dipoles results in reduced built-in stress. These results were confirmed by studies [88, 89, 101] which further found that the detailed arrangement of defects in the GB played an important role. In particular, Wei *et al* [88] found a non-monotonic behaviour of fracture strength with tilt angle for armchair grain boundary configurations, which was also corroborated by a continuum theory in excellent agreement with simulations. Subsequent MD studies have revealed similar results [102–106]. While most studies used straight boundaries, Rasool *et al* [14] and Ophus *et al* [15] showed that more complex boundary structures also typically exhibited a high fracture strength ~ 100 GPa. Using MD it has further been shown that the fracture strength of tilt grain boundaries decreases significantly with increasing temperature [93, 102, 106, 107].

Experimental determination of fracture strength has been carried out by means of nanoindentation measurements. Early results [13, 96] revealed a significantly decreased fracture strength ~ 35 GPa, which was attributed to vacancies and shear stress along the boundaries. However, by using different post-processing methods, it was shown, in accordance with the theoretical predictions, that well-stitched boundaries could have nearly the same fracture strength (≈ 100 GPa) as pristine graphene [84]. Rasool *et al* [108] characterised the grain boundary angles in their measurements, confirming the angle dependence of the fracture strength, and finding high values close to 100 GPa for large angle boundaries. To explain the observed spread in fracture strength in a nanoindentation measurement, Sha *et al* [109] made explicit MD simulations of nanoindentation measurements of polycrystalline graphene, revealing that the relative positioning of the tip and the grain boundaries could yield vastly different fracture strength and different failure paths.

The dependence of fracture strength on tilt angle was predicted by simulations of bi-crystal systems with a single boundary, but more realistic fracture strength simulations of polycrystalline graphene have shown a significant reduction in fracture strength [90] and dependence on grain size [91–93, 95, 110]. In these simulations, failure is typically initiated at the boundary, or more commonly at meeting points between three different grains. The dependence of fracture strength on grain size for the studies in Refs. [91–93, 95] are shown in Fig. 5. Notably, three studies [92, 93, 95] report increasing strength with increasing grain size, while Song *et al* [91] find the opposite trend. The fracture strengths in the study by Kotakoski and Meyer [90] and the paper of Yang *et al* [94], however, showed no significant dependence on grain size.

Nanoindentation measurements by Suk *et al* [111] give support to a decreased fracture strength of polycrystalline graphene, with the fracture strength being smaller for smaller grains. For the comparison between theory and experiment, it is again worth pointing out that most numerical studies have $L \gtrsim l_G \sim 1$ nm, while experimental works are in the regime $L \sim l_G \sim 1$ μ m. In a recent study by Shekhawat and Ritchie [112], a weakest-link argument is used together with MD simulations of $\sim 2 \times 10^4$ grain boundary configurations to obtain a functional form for the fracture strength. They find a scaling for the fracture strength σ , $\sigma - \sigma_0 \propto \nu(l_G/L)^{2/m}$. Here $\sigma_0 = 19.5$ GPa, $\nu = 53.2$ Gpa and $m \approx 10.1$, showing that the fracture strength of large sheets may be significantly lower than previously predicted.

5. Thermal transport properties

The experimental determination of the lattice thermal conductivity κ in graphene remains a matter of debate, since heat transport in such an atomic sheet is sensitive to many details, including the sample dimension and boundaries, point-like or extended defects, and whether the sample is suspended or supported [113]. The estimation of κ is also affected by the experimental protocol, which includes both steady-state measurements [114–117] and measurements in the transient regime where the system evolves from an initial condition of thermal nonequilibrium [118–121]. This wide range of scenarios is reflected in reported experimental values of κ in the interval of 1000 – 5000 $\text{WK}^{-1}\text{m}^{-1}$.

The theoretical prediction of κ is also controversial, since a direct comparison among unlike results is made difficult by different adopted simulation protocols. This includes approximate or exact solutions of the Boltzmann transport equation

[122–126] (BTE) and molecular dynamics (MD) simulations in different flavors, such as equilibrium [127,128] (EMD), nonequilibrium [129] (NEMD), or approach-to-equilibrium [130] (AEMD) formulations. Both full ab initio [125, 126, 131] calculations and MD simulations based on empirical potentials have been published, the latter being mostly based on the Tersoff force field [132] or the reactive empirical bond order potential (REBO) [133]. In summary, theoretical results for κ at room temperature vary in the range $1000 \text{ WK}^{-1}\text{m}^{-1} \leq \kappa \leq 8000 \text{ WK}^{-1}\text{m}^{-1}$ [134].

Finally, we remark that the direct comparison between theoretical predictions and experimental results is often questionable, since most calculations are carried out in idealized situations missing many of the structural details ruling over the experiments. As a matter of fact, real graphene samples, fabricated either by epitaxial film growth [135, 136] or CVD [16, 137, 138], are hardly pristine due to limitations in the growth process and because of substrates and, therefore, they are characterized by defects limiting the size of pristine crystalline domains. Their multi-grain structure, with dimensions down to the micro- and nanoscale, is likely an important pre-existing cause for the wide range of κ values reported above. However, the systematic investigation of the effect of size, shape, and distribution of grains on thermal transport properties is still ongoing [9, 67–69, 139–141].

5.1. Thermal resistance of a single grain boundary

As described in section 2, a single grain boundary can be created in the honeycomb lattice by tilting two crystalline graphene sheets of the same length by a certain angle α (see Fig. 1b). Although such simple geometries correspond to an idealized configuration of a perfectly straight, periodic and isolated grain boundary, they nevertheless represent a paradigmatic situation for investigating the role of GBs in thermal transport.

Both the strain-induced corrugation and the lattice misorientation between the two neighboring grains deeply affect the heat transport along the direction normal to the grain boundary, resulting in an effective GB thermal resistance R_{GB} . This can be described as a series of resistances [67] according to

$$R_{\text{tot}} = \frac{L_{\text{tot}}}{\kappa_{\text{tot}}} = \frac{L_{\text{left}}}{\kappa_{\text{left}}} + R_{\text{GB}} + \frac{L_{\text{right}}}{\kappa_{\text{right}}}, \quad (1)$$

where R_{tot} , L_{tot} , and κ_{tot} are the thermal resistance, length, and thermal conductivity of the total sample, while $L_{\text{left, right}}$ and $\kappa_{\text{left, right}}$ represent the length and thermal conductivity of the left and right crystallites, respectively (see Fig. 1b). By selecting a suitable simulation cell with $L_{\text{right}} = L_{\text{left}} = L_{\text{tot}}/2$ and $\kappa_{\text{left}} = \kappa_{\text{right}} = \kappa_{\text{sg}}$ (here κ_{sg} represents the thermal

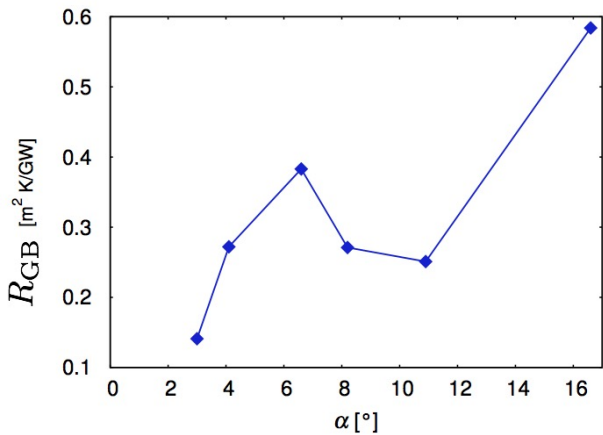


Figure 6. Predicted grain boundary thermal resistance R_{GB} as function of the tilt angle α defining the structure of the grain boundary (see Fig. 1b).

conductivity of a single-grain sample of pristine graphene), Eq. 1 allows one to predict the GB thermal resistance as

$$R_{GB} = \frac{L_{tot}}{2} \left(\frac{1}{\kappa_{tot}} - \frac{1}{\kappa_{sg}} \right). \quad (2)$$

All quantities appearing in Eq. 2 are straightforwardly calculated by an AEMD simulation [68, 130], which provides the value of room-temperature R_{GB} as a function of the tilt angle α . As shown in Fig. 6, the trend is not monotonic, which is likely due to a complex interplay among buckling effects, the occurrence of coordination defects, and bond-network reconstruction. This non-monotonic behavior has not been seen experimentally, but the values of R_{GB} are of the same order of the available experimental data reported in Ref. [52]. Furthermore, the same experiments confirm the general trend of increasing thermal boundary resistance with increasing tilt angle. This is consistent with previous findings reporting an increasing effective thermal conductivity with decreasing mismatch angle [141]. We remark that increased thermal boundary resistance in multi-grain graphene has been attributed to larger out-of-plane buckling [69, 142]. This, however, is not valid for the single isolated GB; the highest thermal boundary resistance occurs for the largest tilt angle where the lowest out-of-plane buckling is observed, as shown in Fig. 1d.

5.2. Thermal conductivity of nanocrystalline graphene

The thermal conductivity in model nanocrystalline graphene samples has been calculated in [68, 69] and the main results are summarized in Fig. 7, where the room-temperature thermal conductivity κ is reported

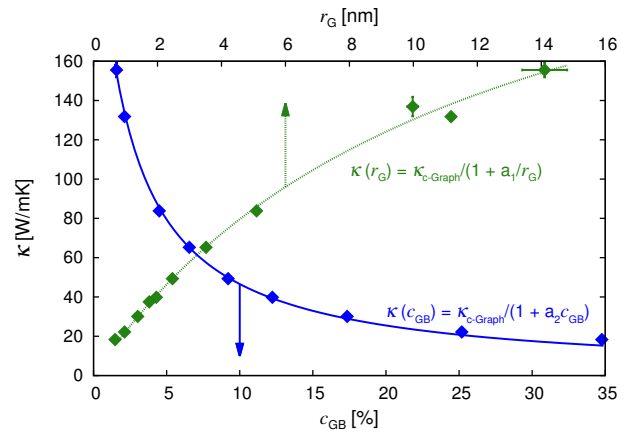


Figure 7. Predicted room-temperature thermal conductivity κ of nanocrystalline graphene as a function of the concentration of atoms in the grain boundaries c_{GB} (blue solid line), and of the average radius of gyration of the graphene grains r_G (green dotted line). Simulations correspond to samples as long as 200 nm.

as a function of the average radius of gyration r_G of the grains (measuring the average granulometry of the nanocrystalline sample) or, equivalently, as a function of the concentration c_{GB} of atoms in the grain boundary (defined as belonging to non-hexagonal rings in the graphene lattice). As expected, samples with a higher density of grain boundaries (or, equivalently, a higher concentration of GB atoms) correspond to smaller thermal conductivity values, consistent with the analysis presented in the previous Section. In all cases, κ is very much reduced with respect to the value 262 W/(m K), found for a single-grain graphene sample with same length. This is in good agreement with Ref. [140] where a reduction of thermal conductivity to about 20 % of the value in pristine graphene is observed for an average grain size of ~ 2.5 nm. This highlights the major role played by GBs in scattering phonons, whose mean free path (MFP) is comparable with the average GB spacing. Based on the accumulation function of the thermal conductivity, the average phonon MFP has been estimated to vary from 451 nm for pristine samples to ~ 30 nm for nanocrystalline ones [68, 69].

An inverse rational function can be used to describe the scaling of κ with r_{GB} and c_{GB} , as shown in Fig. 7 (where $\kappa_{c-Graph}$ is the thermal conductivity of the crystalline grains). A similar argument has been used previously in Ref. [67], where the thermal conductivity of polycrystalline graphene has been calculated by EMD simulations. The good agreement between the calculated data and interpolation functions indicates that the effective thermal conductivity of nanostructured graphene can be estimated considering grain boundaries and grains

as a connection of resistances in series. Given this, the average GB resistance extracted from Fig. 7 is $\sim 0.1 \text{ m}^2 \text{ K/GW}$. This is in reasonably good agreement with the predictions reported in Ref. [139] as well as with the results of the previous Section if one considers that the value extracted from the grain size scaling represents the lower end of the GB resistances in the sample. Further details are found in Ref. [68]. In this scheme, phonon scattering by the GBs is mimicked as an effective interface thermal resistance, while the thermal conductivity of crystalline domains is described by the thermal conductivity of the crystal without grain boundaries.

6. Summary

The scaling analysis of the physical properties of polycrystalline graphene with average grain size has revealed several fundamental features. First, while charge and thermal transport are generally found to scale linearly or sub-linearly with increasing grain size, mechanical properties such as Young's modulus or fracture strength are less dependent on such parameters. Second, electrical measurements have found that the resistivity of individual grain boundaries can vary by up to four orders of magnitude, depending on the quality of the GB and the measurement conditions. However, for large-area polycrystalline graphene the average resistivity of the GBs shows much less variation from sample to sample. Concerning thermal transport, GBs are very efficient phonon scatterers that dramatically reduce the thermal conductivity with respect to pristine graphene. Furthermore, the overall transport properties can be effectively modelled by looking at a nanocrystalline sample as a series of thermal resistances attributed to both grains and GBs. In particular, the predicted GB thermal resistance shows a non-monotonic variation with the tilt angle, arising from the combined effect of interface buckling, coordination defects, and bond reconstruction.

The overall set of information reported here gives a comprehensive picture of the current understanding of the relationship between polycrystalline morphology and the main physical properties of large-area CVD graphene. Ultimately, this can help to assess the usefulness of this material for a variety of applications, from wearable flexible electronics to biosensors to spintronic devices. Additionally, this information can help to guide the production methods and conditions necessary to achieve the material characteristics desired for a particular application. This issue is common to other 2D materials such as MoS₂ where, by combining two-laser Raman thermometry with finite element simulations, it has recently been shown

that heat conduction can be effectively engineered by controlling the nanoscale grain size [143]. For sensing applications smaller grains may be desired, as point defects or grain boundaries could improve the device performance, while for purely electronic applications larger grains would be ideal. Point defects and grain boundaries could also act to tune the interaction with underlying substrates, or as disruptive defects to dictate mean free paths or spin lifetimes [144].

Acknowledgements

AWC, JMK, and SR acknowledge support from the European Union Seventh Framework Programme under grant agreement 604391 Graphene Flagship. LC, AWC and SR acknowledge support from the Severo Ochoa Program (MINECO, Grant SEV-2013-0295). AWC and SR acknowledge support from the Spanish Ministry of Economy and Competitiveness (MAT2012-33911), and Secretaría de Universidades e Investigación del Departamento de Economía y Conocimiento de la Generalidad de Cataluña. LC acknowledges financial support by the Spanish MINECO under grants no. FEDER-FIS2012-37549-C05-02, FEDER-MAT2013-40581-P, TEC2012-31330 and TEC2015-67462-C2-1-R, the Generalitat de Catalunya under grants no. 2014 SGR 301 and 2014 SGR 384, and the Spanish MINECO through the Severo Ochoa Centres of Excellence Program under SEV-2015-0496. AI acknowledges support from the Swedish Research Council (VR).

References

- [1] Gottstein G 2004 *Physical Foundations of Materials Science* (Berlin, Germany: Springer) ISBN 3-540-40139-3
- [2] Seung H S and Nelson D R 1988 *Phys. Rev. A* **38**(2) 1005–1018
- [3] Liu Y and Yakobson B I 2010 *Nano Letters* **10** 2178–2183
- [4] Yazyev O V and Louie S G 2010 *Phys. Rev. B* **81**(19) 195420
- [5] Yazyev O V and Chen Y P 2014 *Nat. Nanotechnol.* **9** 755–767
- [6] Liu T H, Gajewski G, Pao C W and Chang C C 2011 *Carbon* **49** 2306–2317
- [7] Yazyev O V and Louie S G 2010 *Nat. Mater.* **9** 806–809
- [8] Malola S, Häkkinen H and Koskinen P 2010 *Phys. Rev. B* **81** 165447
- [9] Liu H K, Lin Y and Luo S N 2014 *J. Phys. Chem. C* **118** 24797–24802
- [10] Tison Y, Lagoute J, Repain V, Chacon C, Girard Y, Joucken F, Sporcken R, Gargiulo F, Yazyev O V and Rousset S 2014 *Nano Letters* **14** 6382–6386
- [11] Lehtinen O, Kurasch S, Krashennnikov A and Kaiser U 2013 *Nature Communications* **4** 2098
- [12] Kim K, Lee Z, Regan W, Kisielowski C, Crommie M F and Zettl A 2011 *ACS Nano* **5** 2142–2146
- [13] Huang P Y, Ruiz-Vargas C S, van der Zande A M, Whitney W S, Levendorf M P, Kevek J W, Garg S, Alden J S,

- Hustedt C J, Zhu Y, Park J, McEuen P L and Muller D A 2011 *Nature* **469** 389–392
- [14] Rasool H I, Ophus C, Zhang Z, Crommie M F, Yakobson B I and Zettl A 2014 *Nano Lett.* **14** 7057–7063
- [15] Ophus C, Shekhwat A, Rasool H and Zettl A 2015 *Phys. Rev. B* **92**(20) 205402
- [16] Li X, Cai W, An J, Kim S, Nah J, Yang D, Piner R, Velamakanni A, Jung I, Tutuc E, Banerjee S K, Colombo L and Ruoff R S 2009 *Science* **324** 1312–1314
- [17] Mataré H F 1983 *J. Appl. Phys.* **54** 6452–6458
- [18] Yu Q, Jauregui L A, Wu W, Colby R, Tian J, Su Z, Cao H, Liu Z, Pandey D, Wei D, Chung T F, Peng P, Guisinger N P, Stach E A, Bao J, Pei S S and Chen Y P 2011 *Nat. Mater.* **10** 443–449
- [19] Jauregui L A, Cao H, Wu W, Yu Q and Chen Y P 2011 *Solid State Commun.* **151** 1100 – 1104
- [20] Tsen A W, Brown L, Levendorf M P, Ghahari F, Huang P Y, Havener R W, Ruiz-Vargas C S, Muller D A, Kim P and Park J 2012 *Science* **336** 1143–1146
- [21] Clark K W, Zhang X G, Vlassioux I V, He G, Feenstra R M and Li A P 2013 *ACS Nano* **7** 7956–7966
- [22] Fei Z, Rodin A S, Gannett W, Dai S, Regan W, Wagner M, Liu M K, McLeod A S, Dominguez G, Thiemens M, Neto A H C, Keilmann F, Zettl A, Hillenbrand R, Fogler M M and Basov D N 2013 *Nat. Nanotechnol.* **8** 821–825
- [23] Grosse K L, Dorgan V E, Estrada D, Wood J D, Vlassioux I, Eres G, Lyding J W, King W P and Pop E 2014 *Appl. Phys. Lett.* **105** 143109
- [24] Ogawa Y, Komatsu K, Kawahara K, Tsuji M, Tsukagoshi K and Ago H 2014 *Nanoscale* **6** 7288–7294
- [25] Yasaei P, Kumar B, Hantehzadeh R, Kayyalha M, Baskin A, Reppin N, Wang C, Klie R F, Chen Y P, Král P and Salehi-Khojin A 2014 *Nat. Commun.* **5** 4911
- [26] Cummings A W, Duong D L, Nguyen V L, Van Tuan D, Kotakoski J, Barrios Vargas J E, Lee Y H and Roche S 2014 *Adv. Mater.* **26** 5079–5094
- [27] Kochat V, Tiwary C S, Biswas T, Ramalingam G, Hsieh K, Chattopadhyay K, Raghavan S, Jain M and Ghosh A 2016 *Nano Lett.* **16** 562–567
- [28] Kumar S B and Guo J 2012 *Nano Lett.* **12** 1362–1366
- [29] Márk G I, Vancsó P, Hwang C, Lambin P and Biró L P 2012 *Phys. Rev. B* **85** 125443
- [30] Ihnatsenka S and Zozoulenko I V 2013 *Phys. Rev. B* **88** 085436
- [31] Liu Y, Song J, Li Y, Liu Y and Sun Q f 2013 *Phys. Rev. B* **87** 195445
- [32] Vancsó P, Márk G I, Lambin P, Mayer A, Kim Y S, Hwang C and Biró L P 2013 *Carbon* **64** 101 – 110
- [33] Gargiulo F and Yazyev O V 2014 *Nano Lett.* **14** 250–254
- [34] Vancsó P, Márk G I, Lambin P, Mayer A, Hwang C and Biró L P 2014 *Appl. Surf. Sci.* **291** 58 – 63
- [35] Zhang H, Lee G, Gong C, Colombo L and Cho K 2014 *J. Phys. Chem. C* **118** 2338–2343
- [36] Páez C J, Pereira A L C, Rodrigues J N B and Peres N M R 2015 *Phys. Rev. B* **92** 045426
- [37] Hung Nguyen V, Hoang T X, Dollfus P and Charlier J C 2016 *Nanoscale* **8** 11658–11673
- [38] Sun J, Lin N, Li Z, Ren H, Tang C and Zhao X 2016 *RSC Adv.* **6** 1090–1097
- [39] Biró L P and Lambin P 2013 *New J. Phys.* **15** 035024
- [40] Tapasztó L, Nemes-Incze P, Dobrik G, Jae Yoo K, Hwang C and Biró L P 2012 *Appl. Phys. Lett.* **100** 053114
- [41] Koepke J C, Wood J D, Estrada D, Ong Z Y, He K T, Pop E and Lyding J W 2013 *ACS Nano* **7** 75–86
- [42] Cao H, Yu Q, Jauregui L A, Tian J, Wu W, Liu Z, Jalilian R, Benjamin D K, Jiang Z, Bao J, Pei S S and Chen Y P 2010 *Appl. Phys. Lett.* **96** 122106
- [43] Cummings A W, Cresti A and Roche S 2014 *Phys. Rev. B* **90** 161401
- [44] Vlassioux I, Smirnov S, Ivanov I, Fulvio P F, Dai S, Meyer H, Chi M, Hensley D, Datskos P and Lavrik N V 2011 *Nanotechnology* **22** 275716
- [45] Duong D L, Han G H, Lee S M, Gunes F, Kim E S, Kim S T, Kim H, Ta Q H, So K P, Yoon S J, Chae S J, Jo Y W, Park M H, Chae S H, Lim S C, Choi J Y and Lee Y H 2012 *Nature* **490** 235–239
- [46] Yagi K, Yamada A, Hayashi K, Harada N, Sato S and Yokoyama N 2013 *Jpn. J. Appl. Phys.* **52** 110106
- [47] Lee D, Kwon G D, Kim J H, Moyon E, Lee Y H, Baik S and Pribat D 2014 *Nanoscale* **6** 12943–12951
- [48] Venugopal A 2012 Ph.D. thesis The University of Texas at Dallas
- [49] Yang M, Sasaki S, Ohnishi M, Suzuki K and Miura H 2016 *Jpn. J. Appl. Phys.* **55** 04EP05
- [50] Tuan D V, Kotakoski J, Louvet T, Ortmann F, Meyer J C and Roche S 2013 *Nano Lett.* **13** 1730–1735
- [51] Salehi-Khojin A, Estrada D, Lin K Y, Bae M H, Xiong F, Pop E and Masel R I 2012 *Adv. Mater.* **24** 53–57
- [52] Yasaei P, Fathizadeh A, Hantehzadeh R, Majee A K, El-Ghandour A, Estrada D, Foster C, Aksamija Z, Khalili-Araghi F and Salehi-Khojin A 2015 *Nano Lett.* **15** 4532–4540
- [53] Gao L, Xu H, Li L, Yang Y, Fu Q, Bao X and Loh K P 2016 *2D Mater.* **3** 021001
- [54] Banszerus L, Schmitz M, Engels S, Dauber J, Oellers M, Haupt F, Watanabe K, Taniguchi T, Beschoten B and Stampfer C 2015 *Sci. Adv.* **1** e1500222
- [55] Li J, Wang X Y, Liu X R, Jin Z, Wang D and Wan L J 2015 *J. Mater. Chem. C* **3** 3530–3535
- [56] Wu T, Zhang X, Yuan Q, Xue J, Lu G, Liu Z, Wang H, Wang H, Ding F, Yu Q, Xie X and Jiang M 2015 *Nat. Mater.* **15** 43–47
- [57] Lin L, Li J, Ren H, Koh A L, Kang N, Peng H, Xu H Q and Liu Z 2016 *ACS Nano* **10** 2922–2929
- [58] Ryu J, Kim Y, Won D, Kim N, Park J S, Lee E K, Cho D, Cho S P, Kim S J, Ryu G H, Shin H A S, Lee Z, Hong B H and Cho S 2014 *ACS Nano* **8** 950–956
- [59] Novoselov K S, Jiang Z, Zhang Y, Morozov S V, Stormer H L, Zeitler U, Maan J C, Boebinger G S, Kim P and Geim A K 2007 *Science* **315** 1379–1379
- [60] Poirier W and Schopfer F 2010 *Nat. Nanotechnol.* **5** 171–172
- [61] Janssen T J B M, Rozhko S, Antonov I, Tzalenchuk A, Williams J M, Melhem Z, He H, Lara-Avila S, Kubatkin S and Yakimova R 2015 *2D Mater.* **2** 035015
- [62] Shen T, Wu W, Yu Q, Richter C A, Elmquist R, Newell D and Chen Y P 2011 *Appl. Phys. Lett.* **99** 232110
- [63] Lafont F, Ribeiro-Palau R, Han Z, Cresti A, Delvallée A, Cummings A W, Roche S, Bouchiat V, Ducourtieux S, Schopfer F and Poirier W 2014 *Phys. Rev. B* **90** 115422
- [64] Bergvall A, Carlsson J M and Löfwander T 2015 *Phys. Rev. B* **91** 245425
- [65] Lago V D and Torres L E F F 2015 *J. Phys.: Condens. Matter* **27** 145303
- [66] Lehmann T, Ryndyk D A and Cuniberti G 2015 *Phys. Rev. B* **92** 035418
- [67] Mortazavi B, Potschke M and Cuniberti G 2014 *Nanoscale* **6** 3344–3352
- [68] Hahn K R, Melis C and Colombo L 2016 *Carbon* **96** 429–438
- [69] Hahn K R, Melis C and Colombo L 2016 *J. Phys. Chem. C* **120** 3026–3035
- [70] Woessner A, Alonso-Gonzalez P, Lundeberg M B, Gao Y, Barrios-Vargas J E, Navickaite G, Ma Q, Janner D, Watanabe K, Cummings A W, Taniguchi T, Pruneri V, Roche S, Jarillo-Herrero P, Hone J, Hillenbrand R and Koppens F H L 2016 *Nat. Commun.* **7** 10783
- [71] Pirkle A, Chan J, Venugopal A, Hinojos D, Magnuson C W, McDonnell S, Colombo L, Vogel E M, Ruoff R S

- and Wallace R M 2011 *Appl. Phys. Lett.* **99** 122108
- [72] Seifert M, Vargas J E B, Bobinger M, Sachsenhauser M, Cummings A W, Roche S and Garrido J A 2015 *2D Mater.* **2** 024008
- [73] Lee B, Park S Y, Kim H C, Cho K, Vogel E M, Kim M J, Wallace R M and Kim J 2008 *Appl. Phys. Lett.* **92** 203102
- [74] Kim S, Nah J, Jo I, Shahrjerdi D, Colombo L, Yao Z, Tutuc E and Banerjee S K 2009 *Appl. Phys. Lett.* **94** 062107
- [75] Farmer D B, Chiu H Y, Lin Y M, Jenkins K A, Xia F and Avouris P 2009 *Nano Lett.* **9** 4474–4478
- [76] Chan J, Venugopal A, Pirkle A, McDonnell S, Hinojos D, Magnuson C W, Ruoff R S, Colombo L, Wallace R M and Vogel E M 2012 *ACS Nano* **6** 3224–3229
- [77] Fallahazad B, Kim S, Colombo L and Tutuc E 2010 *Appl. Phys. Lett.* **97** 123105
- [78] Fallahazad B, Lee K, Lian G, Kim S, Corbet C M, Ferrer D A, Colombo L and Tutuc E 2012 *Appl. Phys. Lett.* **100** 093112
- [79] Dean C R, Young A F, Merici I, Lee C, Wang L, Sorgenfrei S, Watanabe K, Taniguchi T, Kim P, Shepard K L and Hone J 2010 *Nat. Nanotechnol.* **5** 722–726
- [80] Hao Y, Bharathi M S, Wang L, Liu Y, Chen H, Nie S, Wang X, Chou H, Tan C, Fallahazad B, Ramanarayan H, Magnuson C W, Tutuc E, Yakobson B I, McCarty K F, Zhang Y W, Kim P, Hone J, Colombo L and Ruoff R S 2013 *Science* **342** 720–723
- [81] Hao Y, Wang L, Liu Y, Chen H, Wang X, Tan C, Nie S, Suk J W, Jiang T, Liang T, Xiao J, Ye W, Dean C R, Yakobson B I, McCarty K F, Kim P, Hone J, Colombo L and Ruoff R S 2016 *Nat. Nanotechnol.* **11** 426–431
- [82] Banszerus L, Schmitz M, Engels S, Goldsche M, Watanabe K, Taniguchi T, Beschoten B and Stampfer C 2016 *Nano Lett.* **16** 1387–1391
- [83] Neumann C, Reichardt S, Venezuela P, Drögeler M, Banszerus L, Schmitz M, Watanabe K, Taniguchi T, Mauri F, Beschoten B, Rotkin S V and Stampfer C 2015 *Nat. Commun.* **6** 8429
- [84] Lee G H, Cooper R C, An S J, Lee S, van der Zande A, Petrone N, Hammerberg A G, Lee C, Crawford B, Oliver W, Kysar J W and Hone J 2013 *Science* **340** 1073–1076
- [85] Lee C, Wei X, Kysar J W and Hone J 2008 *Science* **321** 385–388
- [86] Kudin K N, Scuseria G E and Yakobson B I 2001 *Phys. Rev. B* **64**(23) 235406
- [87] Grantab R, Shenoy V B and Rodney R R 2010 *Science* **330** 946–948
- [88] Wei Y, Wu J, Yin H, Shi X, Yang R and Dresselhaus M 2012 *Nat. Mater.* **11** 759–763
- [89] Liu T H, Pao C W and Chang C C 2012 *Carbon* **50** 3465–3472
- [90] Kotakoski J and Meyer J C 2012 *Phys. Rev. B* **85** 195447
- [91] Song Z, Artyukhov V I, Yakobson B I and Xu Z 2013 *Nano Lett.* **13** 1829–1833
- [92] Sha Z D, Quek S S, Pei Q X, Liu Z S, Wang T J, Shenoy V B and W Z Y 2014 *Sci. Rep.* **4** 5991
- [93] Chen M Q, Quek S S, Sha Z D, Chiu C H, Pei Q X and W Z Y 2015 *Carbon* **85** 135–146
- [94] Yang Z, Huang F, Sun Y, Xu K and Chu P K 2015 *Mater. Sci. Eng. B* **198** 95–101
- [95] Mortazavi B and Cuniberti G 2014 *Nanotechnology* **25** 215704
- [96] Ruiz-Vargas C S, Zhuang H L, Huang P Y, van der Zande A M, Garg S, McEuen P L, Muller D A, Hennig R G and Park J 2011 *Nano Lett.* **11** 2259–2263
- [97] Zandiatashbar A, Lee G H, An S J, Lee S, Mathew N, Terrones M, Hayashi T, Picu C R, Hone J and Koratkar N 2014 *Nat. Commun.* **5** 3186
- [98] Lopez-Polin G, Gomez-Navarro C, Parente V, Guinea F, Katsnelson M I, Perez-Murano F and Gomez-Herrero J 2015 *Nat. Phys.* **11**(1) 26–31
- [99] Liu F, Ming P and Li J 2007 *Phys. Rev. B* **76**(6) 064120
- [100] Rajasekaran G, Narayanan P and Parashar A 2015 *Crit. Rev. Solid State Mat. Sci.* **41** 47–71
- [101] Zhang J, Zhao J and Lu J 2012 *ACS Nano* **6** 2704 – 2711
- [102] Yi L, Yin Z, Zhang Y and Chang T 2013 *Carbon* **51** 373 – 380
- [103] Jhon Y I, Chung P S, Smith R, Min K S, Yeom G Y and Jhon M S 2013 *RSC Adv.* **3** 9897–9903
- [104] Wu J and Wei Y 2013 *J. Mech. Phys. Solids* **61** 1421–1432
- [105] Han J, Ryu S, Sohn D and Im S 2014 *Carbon* **68** 250 – 257
- [106] Yang B, Wang S, Guo Y, Yuan J, Si Y, Zhanga S and Chen H 2014 *RSC Adv.* **4** 54677–54683
- [107] Zhang H, Duan Z, Zhang X, Liu C, Zhang J and Zhao J 2013 *Phys. Chem. Chem. Phys.* **15** 11794–11799
- [108] Rasool H I, Ophus C, Klug W S, Zettl A and Gimzewski J K 2013 *Nat. Commun.* **4** 2811
- [109] Sha Z D, Wan Q, Pei Q X, Quek S S, Liu Z S, Zhang Y W and Shenoy V B 2014 *Sci. Rep.* **4** 7437
- [110] Cao A and Qu J 2013 *Appl. Phys. Lett.* **102** 071902
- [111] Suk J W, Mancevski V, Yufen H, Liechti K and Ruoff R S 2015 *Phys. Status Solidi RRL* **9** 564–569
- [112] Shekhawat A and Ritchie R O 2016 *Nat. Commun.* **7** 10546
- [113] Balandin A A 2011 *Nat. Mater.* **10** 569–581
- [114] Balandin A A, Gosh S, W B, Calizo I, Teweldebrhan D, Miao F and Lau C N 2008 *Nano Lett.* **8** 902–907
- [115] Gosh S, Calizo I, Teweldebrhan D, Pokatilov E P, Nika D L, Balandin A A, Bao W, Miao F and Lau C N 2008 *Appl. Phys. Lett.* **92** 151911
- [116] Lee J U, Yoon D, Kim H, Lee S W and Cheong H 2011 *Phys. Rev. B* **83** 081419
- [117] Jang W, Bao W, Jing L, Lau C N and Dames C 2013 *Appl. Phys. Lett.* **103** 133102
- [118] Jang W, Chen Z, Bao W, Lau C N and Dames C 2010 *Nano Lett.* **10** 3909–3913
- [119] Cabrera H, Mendoza D, L B J and et al 2015 *J. Phys. D: Appl. Phys.* **48** 465501
- [120] Guo J Q, Wang X W, Geohagan D B and Eres G 2008 *Funct. Mater. Lett.* **1** 71
- [121] Guo J Q, Wang X W, Geohagan D B, Eres G and Vincent C 2008 *J. Appl. Phys.* **103** 113505
- [122] Lindsay L, Broido D A and Mingo N 2010 *Phys. Rev. B* **82** 115427
- [123] Lindsay L, Broido D A and Mingo N 2011 *Phys. Rev. B* **83** 235428
- [124] Singh D, Murthy J Y and Fisher T S 2011 *J. Appl. Phys.* **11** 044317
- [125] Lindsay L, Li W, Carrete J, Mingo N, Broido D A and Reinecke T L 2014 *Phys. Rev. B* **89** 155426
- [126] Cepellotti A, Fugallo G, Paulatto L, Lazzeri M, Mauri F and Marzari N 2015 *Nat. Commun.* **6** 6400
- [127] Pereira L F C and Donadio D 2013 *Phys. Rev. B* **87** 125424
- [128] Fan Z, Pereira L F C, Wang H Q, Zheng J C, Donadio D and Harju A 2015 *Phys. Rev. B* **92** 094301
- [129] Xu X, Pereira L F C, Wang Y, Wu J, Zhang K, Zhao X, Bae S, Bui C T, Xie R, Thing J T L, Hong B H, Loh K P, Donadio D, Li B and Özyilmaz B 2014 *Nat. Commun.* **5** 3689
- [130] Barbarino G, Melis C, and Colombo L 2015 *Phys. Rev. B* **91** 035416
- [131] Fugallo G, Cepellotti A, Paulatto L, Lazzeri M, Marzari N and Mauri F 2014 *Nano Lett.* **14** 6109
- [132] Lindsay L and Broido D A 2010 *Phys. Rev. B* **81** 205441
- [133] Brenner D W, Shenderova O A, Harrison J A, Stuart S J, Ni B and Sinnott S B 2002 *J. Phys.: Condens. Matter* **14** 783–802

- [134] Nika D L and Balandin A A 2012 *J. Phys.: Condens. Matter* **24** 233203
- [135] Berger C, Song Z, Li X, Wu X, Brown N, Naud C, Mayou D, Li T, Hass J, Marchenkov A N, Conrad E H, First P N and De Heer W A 2006 *Science* **312** 1191–1196
- [136] Hass J, De Heer W A and Conrad E H 2008 *J. Phys.: Condens. Matter* **20** 323202
- [137] Ding X, Ding G, Xie X, Huang F and Jiang M 2011 *Carbon* **49** 2522–2525
- [138] Su C Y, Lu A Y, Wu C Y, Li Y T, Liu K K, Zhang W, Lin S Y, Juang Z Y, Zhong Y L, Chen F R and Li L J 2011 *Nano Lett.* **11** 3612–3616
- [139] Bagri A, Kim S P and Ruoff R S 2011 *Nano Letters* **11**(9) 3917
- [140] Wu P H, Quek S S, Sha Z D, Dong Z L, Liu X J, Zhang G, Pei Q X and Zhang Y W 2014 *Journal of Applied Physics* **116**(20) 204303
- [141] Wang Y, Song Z and Xu Z 2014 *Journal of Materials Research* **29**(3) 362
- [142] Helgee E E and Isacsson A 2014 *Phys. Rev. B* **90** 045416
- [143] Sledzinska M, Graczykowski B, Placidi M, Saleta Reig D, Sachat A E, Reparaz J S, Alzina F, Mortazavi B, Quey R, Colombo L, Roche S and Sotomayor Torres C M 2016 *2D Materials* **3** 035016
- [144] Roche S, Åkerman J, Beschoten B, Charlier J C, Chshiev M, Dash S P, Dlubak B, Fabian J, Fert A, Guimarães M, Guinea F, Grigorieva I, Schönenberger C, Seneor P, Stampfer C, Valenzuela S O, Waintal X and van Wees B 2015 *2D Mater.* **2** 030202